Journal of Computational Physics 466 (2022) 111367

Contents lists available at ScienceDirect

Journal of Computational Physics

www.elsevier.com/locate/jcp

An immersed boundary projection method for solving the fluid-rigid body interaction problems

Kian Chuan Ong [a,*], Yunchang Seol [b], Ming-Chih Lai [c]

[a] Fields Institute for Research in Mathematical Sciences, 222 College Street, Toronto, Ontario, M5T3J1 Canada
[b] Department of Mathematics, Kyungpook National University, Daegu 41566, Republic of Korea
[c] Department of Applied Mathematics, National Yang Ming Chiao Tung University, 1001, Ta Hsueh Road, Hsinchu 300, Taiwan

ARTICLE INFO

Article history:
Received 1 September 2021
Received in revised form 24 April 2022
Accepted 31 May 2022
Available online 20 June 2022

Keywords:
Immersed boundary projection method
Fluid-rigid body interactions
Fractional step method
Cauchy's stress theorem
Rigid body dynamics

ABSTRACT

We develop an immersed boundary projection method for solving the Naiver-Stokes equations and Newton-Euler equations to simulate the fluid-rigid body interactions in two and three dimensions. A novel fractional step algorithm is introduced for which fast solvers can be applied by exploiting the algebraic structure of the underlying schemes. The Navier-Stokes equations are decoupled while the Newton-Euler equations are solved simultaneously with a constraint equation of the immersed boundary force density. In contrast to previous works, the present method preserves both the fluid incompressibility and the kinematic constraint of the rigid body dynamics at a discrete level simultaneously while maintaining numerical stability. We demonstrate the numerical results of the present method involving spherical and spheroidal rigid bodies with a moderate range of density ratios, which are congruent with the results in the literature.

1. Introduction

The immersed boundary (IB) method [1] is a classical numerical method for simulating the fluid-rigid body interactions (FRI). The fundamental principle of the IB method is based on a Lagrangian description of the rigid body interface immersed in an Eulerian description of the fluid domain. The fluid and rigid body interactions are coupled through the convolution with a regularized delta function. Hence, the IB method requires minimal geometric information to handle complex moving rigid bodies without sophisticated mesh generation [2]. The numerical study of FRI is widely utilized in various engineering applications, including aerospace, energy, biomedical, etc. The transient dynamics are characterized by the constraints, i.e., kinematic no-slip boundary condition, Cauchy's stress theorem, and fluid incompressibility, which pose a range of challenges in developing robust numerical schemes in terms of computational cost, accuracy, and numerical stability. In general, a majority of the proposed IB methods for solving FRI problems are the extension of the baseline IB methods for static and moving rigid bodies (one-way coupling) by incorporating the Newton-Euler equations to account for the rigid body dynamics. In the context of the IB formulation that uses a regularized delta kernel for the coupling of fluid and rigid body dynamics, a plethora of algorithms have been developed due to its simplicity and robustness. The fundamental difference between these proposed algorithms can be classified into several categories. For instance, direct forcing IB methods [3–9], penalty IB methods [10], and projection-based methods [11–15].

* Corresponding author.
E-mail addresses: kong@fields.utoronto.ca (K.C. Ong), ycseol@knu.ac.kr (Y. Seol), mclai@math.nctu.edu.tw (M.-C. Lai).

https://doi.org/10.1016/j.jcp.2022.111367
0021-9991/

The direct forcing approach [3] employs an explicit formulation of the FRI force to satisfy the constraint directly. The discrete delta kernel is utilized for the interaction of the fluid velocity and IB force density between the Eulerian and Lagrangian representations. It is observed that the approach does not enforce the kinematic constraint exactly and does not maintain the numerical stability when the density ratio is close to unity. An iterative procedure [6] is developed to enforce the kinematic constraint and the boundary conditions at the rigid body interface. On the other hand, stabilized schemes [6,7] have been proposed to extend the accessible density close to zero. However, these improvements impose additional algorithm complexity and computational overhead. Recently, a non-iterative procedure for the explicit forcing approach is proposed for spherical [8] and spheroid rigid bodies [9] to address the aforementioned drawbacks. The kinematic constraint of the rigid body dynamics and boundary conditions at the interface can be enforced while maintaining the numerical stability for arbitrary density ratio.

The penalty formulation has been adopted in the IB framework to impose the rigid body constraint as a velocity constraint for the Navier-Stokes equations [2]. The fundamental principle is to apply the constraint residual to act as a penalty force. This concept is further utilized to solve FRI problems [10] in 2D and 3D. However, there exist several drawbacks to the penalty IB formulation. Firstly, the penalty force inevitably introduces an empirical penalization parameter that highly depends on the problems. Achieving the optimal value of the parameter remains a challenging topic since it varies spatially and temporally throughout the simulation. In practice, the numerical stability is severely jeopardized due to the high value of the parameter. The computational time step is therefore restricted to $O(h^2)$ or higher, where h is the mesh size. Hence, satisfying the rigid body constraints consistently up to the local truncation error or a prescribed tolerance while maintaining numerical stability remains a critical numerical issue in the context of the IB method.

The projection-based method has been proposed by Taira and Colonius [16] for simulating incompressible flows over moving rigid bodies, based on the fractional step analysis of Perot [18] applied to the IB framework. The primary principle is to derive the linear system into a block-LU decomposition. A modified Poisson equation is required to solve the coupled singular IB force and fluid pressure, which act as the Lagrange multipliers to satisfy rigid body constraints and fluid incompressibility. A nullspace approach [17] based on the vorticity-stream function eliminates the need to solve the modified Poisson equation for fluid pressure. In [11], the nullspace approach is coupled with Newton-Euler equations to solve rigid body dynamics iteratively with a relaxation scheme. Similarly, an extension is proposed to solve the FRI problems involving thin deforming body dynamics [13]. Such nullspace approach is recently extended by [15] to solve the FRI problems by discretizing the coupled system implicitly in the target-fixed non-inertial frame. The original IBPM [16] is further extended by [12] to incorporate the rigid body dynamics by solving the Newton-Euler equations using the primitive variables. The fluid motion and rigid body motion are implicitly coupled, and stable solutions for very small density ratios are obtained.

The main objective of the present study is to develop an immersed boundary projection method (IBPM) for solving the FRI problems in 2D and 3D involving spherical and spheroidal rigid bodies with a moderate range of density ratios. Based on the fractional analysis [18,16], we propose a numerical algorithm to decouple the Navier-Stokes equations and Newton-Euler equations while maintaining numerical stability, accuracy, and efficiency. The remainder of the present study is organized as follows. In Section 2, we define the governing equations of a rigid body immersed in an incompressible viscous fluid domain. In Section 3, we describe the details of the computational domain, i.e., staggered finite difference framework and the interface representation by a triangulated surface composed of Lagrangian markers, followed by the numerical discretization of the governing equations. In Section 4, we derive the numerical algorithm of the IBPM for solving the FRI problems based on the fractional analysis [18,16]. Then, we demonstrate the grid convergence rates of Navier-Stokes solver and IBPM in Section 5. After the numerical validation, we further explore the dynamics of FRI in a quiescent fluid and shear flow by varying the critical parameters. The numerical results are justified by comparing to the existing analytical and numerical results obtained from the literature. Finally, we summarize the conclusion of the present study in Section 6.

2. Governing equations of motion

The fluid-rigid body interaction problem can be described by the Navier-Stokes equations for the incompressible fluid flow and the Newton-Euler equations for the combined translational and rotational dynamics of a rigid body [19], i.e.

$$\rho_f\left(\frac{\partial \mathbf{u}}{\partial t}+(\mathbf{u}\cdot\nabla)\mathbf{u}-\nu\Delta\mathbf{u}+\nabla p\right)=\int_{\partial\Omega_s}\mathbf{F}(\alpha,\beta,t)\,\delta\left(\mathbf{x}-\mathbf{X}(\alpha,\beta,t)\right)\mathrm{d}A \quad \text{in } \Omega_f, \tag{1}$$

$$\nabla\cdot\mathbf{u}=0, \quad \text{in } \Omega_f, \tag{2}$$

$$\frac{\partial \mathbf{X}(\alpha,\beta,t)}{\partial t}=\int_{\Omega_f}\mathbf{u}(\mathbf{x},t)\delta\left(\mathbf{x}-\mathbf{X}(\alpha,\beta,t)\right)\mathrm{d}\mathbf{x}=\mathbf{U}_c+Q(t)\boldsymbol{\omega}_c\times\left(\mathbf{X}(\alpha,\beta,t)-\mathbf{X}_c\right) \quad \text{on } \partial\Omega_s, \tag{3}$$

$$M_s\frac{\mathrm{d}\mathbf{U}_c}{\mathrm{d}t}=-\int_{\partial\Omega_s}\mathbf{F}(\alpha,\beta,t)\mathrm{d}A+\left(\rho_s-\rho_f\right)|\Omega_s|\,\mathbf{g}, \tag{4}$$

$$\mathbf{I}_s\frac{\mathrm{d}\boldsymbol{\omega}_c}{\mathrm{d}t}+\boldsymbol{\omega}_c\times\mathbf{I}_s\boldsymbol{\omega}_c=-Q^{\mathsf{T}}(t)\int_{\partial\Omega_s}\left(\mathbf{X}(\alpha,\beta,t)-\mathbf{X}_c\right)\times\mathbf{F}(\alpha,\beta,t)\mathrm{d}A, \tag{5}$$

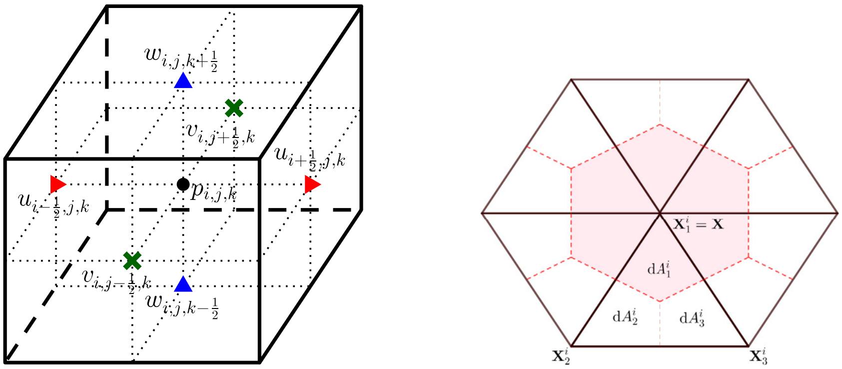

(a) Staggered finite difference grid (b) Surface triangulation

Fig. 1. Discretization of computational domain. (a) Fluid velocity (u, v, w) and fluid pressure p defined on the staggered grid. (b) A 1-ring of triangles around a vertex $\mathbf{X} = \mathbf{X}_1^i$, and the effective area (colored in red) of the vertex $\mathbf{X}$ on triangulated closed interface. (For interpretation of the colors in the figure(s), the reader is referred to the web version of this article.)

where $\mathbf{u}(\mathbf{x}, t) = (u, v, w)$ is the fluid velocity, $p(\mathbf{x}, t)$ is the fluid pressure, ρ_f is the fluid density, and ν is the kinematic viscosity. Here, $\mathbf{x} = (x, y, z)$ is the Cartesian coordinates in the fluid domain Ω_f. The pressure p acts as the Lagrange multiplier to enforce the fluid incompressibility, i.e. Equation (2) on the entire fluid domain Ω_f. The boundary of the rigid body $\partial\Omega_s$ is represented by a set of Lagrangian markers $\mathbf{X}(\alpha, \beta, t)$ with two parameters α and β. $M_s = \rho_s |\Omega_s|$ is the mass of the rigid body where ρ_s is its density. The moment of inertia tensor $\mathbf{I}_s \in R^{3\times3}$ of the rigid body is given by $\mathbf{I}_s = \int_{\Omega_s} \rho_s(|\boldsymbol{\Gamma}|^2 \mathbf{I} - \boldsymbol{\Gamma} \otimes \boldsymbol{\Gamma})\mathrm{d}\mathbf{x}$ where $\boldsymbol{\Gamma} = \mathbf{x} - \mathbf{X}_c$. $\mathbf{U}_c(\mathbf{X}_c, t)$ is the translational velocity of the rigid body at the its center of mass $\mathbf{X}_c$, while $\boldsymbol{\omega}_c(\mathbf{X}_c, t) = (\omega_x, \omega_y, \omega_z)$ is the angular velocity in the body-fixed non-inertial frame. Solving Equation (5) for the angular velocity $\boldsymbol{\omega}_c$ in the non-inertial frame is favorable since the time-derivative of the moment of inertia tensor is absent in this case. Rotating the vector in the non-inertial frame to inertial frame or vice versa can be done using the orthogonal rotation matrix $Q(t)$ which we will further elaborate in the following section. Note that, the Navier-Stokes equations and the Newton-Euler equations are coupled through the IB force density $\mathbf{F}(\alpha, \beta, t)$. Lastly, $\mathbf{g}$ is the gravitational acceleration acting on the massive rigid body. Of course, Equations (1) to (5) should be accompanied with suitable initial and boundary conditions as we shall describe specifically later in numerical experiments.

3. Numerical discretization

In the present study, the fluid variables are defined on the staggered finite difference grid in a computational rectangular domain $\Omega_f = [a, b] \times [c, d] \times [e, f]$ as shown in Fig. 1(a). The pressure p is defined at the cell-center $\mathbf{x} = (x_i, y_j, z_k) = (a + (i - 1/2)\Delta x, c + (j - 1/2)\Delta y, e + (k - 1/2)\Delta z)$, $i = 1, 2, \cdots, N_x$, $j = 1, 2, \cdots, N_y$, and $k = 1, 2, \cdots, N_z$, while the velocity components u, v, and w are defined at cell-edges $(x_{i-1/2}, y_j, z_k) = (a + (i - 1)\Delta x, c + (j - 1/2)\Delta y, e + (k - 1/2)\Delta z)$, $(x_i, y_{j-1/2}, z_k) = (a + (i - 1/2)\Delta x, c + (j - 1)\Delta y, e + (k - 1/2)\Delta z)$, and $(x_i, y_j, z_{k-1/2}) = (a + (i - 1/2)\Delta x, c + (j - 1/2)\Delta y, e + (k - 1)\Delta z)$, respectively. For brevity, we assume a uniform grid size of $h = \Delta x = \Delta y = \Delta z$. To represent the immersed rigid body Ω_s and its surface $\partial\Omega_s$, we define an embedded domain $\Omega_s \subset \Omega_f$ and approximate by a triangulated surface composed of the T-number of triangles and the K-number of vertices. Therefore k-th vertex or Lagrangian marker is denoted by $\mathbf{X}_k$ for all $k \in \{1, 2, \cdots, K\}$ and the three vertices which form the i-th triangle for all $i \in \{1, 2, \cdots, T\}$ are denoted by $\mathbf{X}_1^i$, $\mathbf{X}_2^i$, and $\mathbf{X}_3^i$. Given k-th vertex, we set $\mathbf{X}_k = \mathbf{X}_1^i$, and subsequently define $\mathbf{X}_2^i$ and $\mathbf{X}_3^i$ accordingly in the counter clockwise direction, so that the unit normal vector of the i-th triangle $\mathbf{n}^i = \frac{(\mathbf{X}_2^i - \mathbf{X}_1^i)\times(\mathbf{X}_3^i - \mathbf{X}_1^i)}{(\left|\mathbf{X}_2^i - \mathbf{X}_1^i)\times(\mathbf{X}_3^i - \mathbf{X}_1^i)\right|}$ points to the outward direction of the surface. Referring to Fig. 1(b), let a set of $T(\mathbf{X}_k)$ triangles form the 1-ring surrounding $\mathbf{X}_k$, then the effective local area at the vertex $\mathbf{X}_k$ is evaluated by

$$\Delta A(\mathbf{X}_k) = \sum_{i \in T(\mathbf{X}_k)} \frac{\mathrm{d}A^i}{3}, \quad \mathrm{d}A^i = \frac{1}{2}\left|\left(\mathbf{X}_2^i - \mathbf{X}_1^i\right) \times \left(\mathbf{X}_3^i - \mathbf{X}_1^i\right)\right|.$$

In the present study, the governing equations (1)-(5) are discretized using backward Euler method as follows,

$$\frac{\mathbf{u}^{n+1} - \mathbf{u}^n}{\Delta t} + \left(\mathbf{u}^n \cdot \nabla_h\right)\mathbf{u}^n - \nu\Delta_h \mathbf{u}^{n+1} + \nabla_h p^{n+1} = \frac{1}{\rho_f}\sum_{k=1}^{K} \mathbf{F}_k^{n+1}\delta_h\left(\mathbf{x} - \mathbf{X}_k^n\right)\Delta A(\mathbf{X}_k^n), \tag{6}$$

$$\nabla_h \cdot \mathbf{u}^{n+1} = 0, \tag{7}$$

$$\sum_{\mathbf{x}} \mathbf{u}(\mathbf{x})^{n+1} \delta_h \left(\mathbf{x} - \mathbf{X}_k^n\right) h^3 = \mathbf{U}_c^{n+1} + Q \left(\boldsymbol{\omega}_c^{n+1} \times \boldsymbol{\Gamma}_k^0\right) \quad \forall k, \tag{8}$$

$$M_e \frac{\mathbf{U}_c^{n+1} - \mathbf{U}_c^n}{\Delta t} = -\sum_{k=1}^{K} \mathbf{F}_k^{n+1} \Delta A(\mathbf{X}_k^n) + \left(\rho_s - \rho_f\right) |\Omega_s| \, \mathbf{g}, \tag{9}$$

$$\mathbf{I}_e \frac{\boldsymbol{\omega}_c^{n+1} - \boldsymbol{\omega}_c^n}{\Delta t} + \boldsymbol{\omega}_c^n \times \mathbf{I}_e \boldsymbol{\omega}_c^n = -\sum_{k=1}^{K} \boldsymbol{\Gamma}_k^0 \times Q^{\mathsf{T}} \mathbf{F}_k^{n+1} \Delta A(\mathbf{X}_k^n). \tag{10}$$

The spatial operators ∇_h and Δ_h are the second-order central difference approximations to the gradient and Laplacian on the staggered finite difference grid, respectively. $\nabla_h \cdot$ is the discrete divergence operator corresponding to the discrete gradient. For the nonlinear convective term, the skew-symmetric form is explicitly applied as $\left(\mathbf{u}^n \cdot \nabla_h\right) \mathbf{u}^n = \frac{1}{2}\left(\mathbf{u}^n \cdot \nabla_h\right) \mathbf{u}^n + \frac{1}{2} \nabla_h \cdot \left(\mathbf{u}^n \otimes \mathbf{u}^n\right)$. We employ the effective mass $M_e = (1 - \rho_f/\rho_s) M_s$ and effective moment of inertia tensor $\mathbf{I}_e = (1 - \rho_f/\rho_s) \mathbf{I}_s$ for the rigid body to account for the internal fluid effect in Ω_s [3]. The radius from the rigid body's surface to its center is defined as $\boldsymbol{\Gamma}_k = \mathbf{X}_k - \mathbf{X}_c$, thus $\boldsymbol{\Gamma}_k^0 = \mathbf{X}_k^0 - \mathbf{X}_c^0$ is defined at the initial time.

In Eqs. (8) and (10), Q is an orthogonal matrix denotes the rotation from body-fixed frame to inertial frame using a unit quaternion representation. Consider a rotation of angle α by the right-hand rule about an axis represented by a unit vector $\mathbf{n}$, the unit quaternion representation for the rotation is defined as in [20]

$$\mathbf{q} = [q_0, q_1, q_2, q_3]^{\mathsf{T}} = \left[\cos\frac{\alpha}{2}, n_x \sin\frac{\alpha}{2}, n_y \sin\frac{\alpha}{2}, n_z \sin\frac{\alpha}{2}\right]^{\mathsf{T}}, \quad |\mathbf{q}|^2 = q_0^2 + q_1^2 + q_2^2 + q_3^2 = 1.$$

Therefore Q is defined as

$$Q = \begin{bmatrix} q_0^2 + q_1^2 - q_2^2 - q_3^2 & 2q_1q_2 - 2q_0q_3 & 2q_0q_2 + 2q_1q_3 \\ 2q_0q_3 + 2q_1q_2 & q_0^2 - q_1^2 + q_2^2 - q_3^2 & 2q_2q_3 - 2q_0q_1 \\ 2q_1q_3 - 2q_0q_2 & 2q_0q_1 + 2q_2q_3 & q_0^2 - q_1^2 - q_2^2 + q_3^2 \end{bmatrix}. \tag{11}$$

Quaternions are elegant and relatively stable when used numerically to represent rotation compared to rotation matrices based on Euler angles. In addition, they avoid the drawback of gimbal lock caused by the Euler angles [20]. We note that employing the unit quaternion in the governing equations for the rotation representation yields a block skew-symmetric linear system, as we will see later in the following section. In practice, the Euler angles $\boldsymbol{\Phi}$ can be evaluated from the quaternion via the relation [20]

$$\boldsymbol{\Phi} = \begin{bmatrix} \phi_x \\ \phi_y \\ \phi_z \end{bmatrix} = \begin{bmatrix} \tan^{-1}\left(\frac{2(q_0q_1 + q_2q_3)}{1 - 2(q_1^2 + q_2^2)}\right) \\ \sin^{-1}\left(2(q_0q_2 - q_1q_3)\right) \\ \tan^{-1}\left(\frac{2(q_0q_3 + q_1q_2)}{1 - 2(q_2^2 + q_3^2)}\right) \end{bmatrix}.$$

The time derivative of the quaternion is then evaluated by the angular velocity components $\boldsymbol{\omega}_c = (\omega_x, \omega_y, \omega_z)$ and the quaternion itself, given by

$$\frac{\mathrm{d}\mathbf{q}}{\mathrm{d}t} = \frac{1}{2} \begin{bmatrix} 0 & -\omega_x & -\omega_y & -\omega_z \\ \omega_x & 0 & \omega_z & -\omega_y \\ \omega_y & -\omega_z & 0 & \omega_x \\ \omega_z & \omega_y & -\omega_x & 0 \end{bmatrix} \begin{bmatrix} q_0 \\ q_1 \\ q_2 \\ q_3 \end{bmatrix} = W\mathbf{q}. \tag{12}$$

It is necessary to preserve the constraint of a unit quaternion $|\mathbf{q}| = 1$ to resolve the rigid body dynamics. In order to enforce the constraint, re-normalization is usually required at each time-step. However, this approach inevitably alters the relation between the four parameters of the quaternion, and modifies the rotation it represents [21]. To preserve the constraint without re-normalization, Equation (12) is evaluated by using the method of integrating factor and the backward Euler time integration, so the resulting exponential map is expressed by the Taylor series [22], i.e.

$$\begin{aligned} \mathbf{q}^{n+1} &= \exp\left(W^{n+1} \Delta t\right) \mathbf{q}^n \\ &= \left[\cos\left(\left|\boldsymbol{\omega}_c^{n+1}\right| \Delta t/2\right) \mathbf{I} + \frac{2}{\left|\boldsymbol{\omega}_c^{n+1}\right|} \sin\left(\left|\boldsymbol{\omega}_c^{n+1}\right| \Delta t/2\right) W^{n+1}\right] \mathbf{q}^n. \end{aligned} \tag{13}$$

It is important to mention that aforementioned numerical scheme (6)-(10) is a linearly semi-implicit scheme though the governing equations (1)-(5) are nonlinear. The convective terms $(\mathbf{u} \cdot \nabla_h) \, \mathbf{u}$ and $\boldsymbol{\omega}_c \times \mathbf{I}_e \boldsymbol{\omega}_c$ are discretized explicitly. While the IB force is discretized implicitly, the spreading operator and the interpolation operator are linearized by lagging one time step Δt for the Lagrangian markers from $t=(n+1)\Delta t$ to $t=n\Delta t$. Therefore, lagging the spreading and interpolation operators results a linear system of equations instead of the nonlinear one. In the next section, we focus on the development of an efficient IBPM to solve the linearly semi-implicit system.

4. Immersed boundary projection method

The main objective of the present study is to develop an IBPM to solve the aforementioned discretized system of equations (Equations (6) to (10)) for $\mathbf{u}$, p, $\mathbf{F}$, $\mathbf{U}_c$, and $\boldsymbol{\omega}_c$ efficiently. The present method follows the algebraic approach based on the fractional step analysis of Perot [18] applied to the IB framework by Taira and Colonius [16], for simulating incompressible flows over moving rigid body. The primary principle is to cast the entire linear system into a block-LU decomposition and then make appropriate approximations to obtain several fractional steps that can be efficiently solved. To facilitate the numerical algorithm development, we consider first the governing equations in linear operator form as follows

$$H\mathbf{u}^{n+1}+Gp^{n+1}+E_S\mathbf{F}^{n+1}=\mathbf{r}+bc_1, \tag{14}$$

$$D\mathbf{u}^{n+1}\equiv -G^{\intercal}\mathbf{u}^{n+1}=bc_2, \tag{15}$$

$$E_I\mathbf{u}^{n+1}+R\boldsymbol{\Theta}^{n+1}=0, \quad \boldsymbol{\Theta}^{n+1}=\left[\mathbf{U}_c^{n+1} \;\; \boldsymbol{\omega}_c^{n+1}\right]^{\intercal}, \tag{16}$$

$$M\boldsymbol{\Theta}^{n+1}+E_R\mathbf{F}^{n+1}=\mathbf{s}, \tag{17}$$

where $H=\frac{1}{\Delta t}I-\nu L$ is the discrete modified Helmholtz operator, L is the discrete Laplacian operator, G is the discrete gradient operator, $D\equiv -G^{\intercal}$ is the discrete divergence operator, and $\mathbf{r}=\frac{\mathbf{u}^n}{\Delta t}-\left(\mathbf{u}^n\cdot\nabla_h\right)\mathbf{u}^n$ is the explicit source term of the Navier-Stokes equations including the nonlinear convective term. The term bc_1 is the boundary condition resulting from the Helmholtz operator, whereas bc_2 is the boundary condition resulting from the divergence operator. E_I is the discrete interpolation operator that interpolates velocity components defined at the cell-edges onto the Lagrangian markers. E_S is the discrete spreading operator that regularizes the singular surface force $\mathbf{F}$ over the adjacent Eulerian grid. R is the discrete rigid body motion operators related to the translation and rotational dynamics. E_R represents the discrete stress tensor operator related to the force and torque components acting on the rigid body. M contains the effective mass M_e, effective moment of inertia tensor $\mathbf{I}_e$, and the discrete time derivative operator. The vector $\mathbf{s}$ represents the explicit source term of the Newton-Euler equations.

Following the fractional step analysis [16] in the context of IB framework, we apply the transformed forcing function $\mathbf{F}\equiv -(E_IE_S)^{-1}E_IE_I^{\intercal}\hat{\mathbf{F}}=\left(\rho_f h^3/\Delta A\right)\hat{\mathbf{F}}$. Note that the Newton-Euler equations are also scaled accordingly, i.e. $\hat{M}\boldsymbol{\Theta}^{n+1}+\hat{E}_R\hat{\mathbf{F}}^{n+1}=\hat{\mathbf{s}}$. We drop the overhead symbol $(\hat{\cdot})$ hereafter for the ease of presentation. Since $E_I\equiv -S^{\intercal}$ and $\hat{E}_R\equiv -R^{\intercal}$, Equations (14) to (17) produce a block skew-symmetric algebraic system of equations in the following form

$$\begin{bmatrix} H & G & S & 0 \\ -G^{\intercal} & 0 & 0 & 0 \\ -S^{\intercal} & 0 & 0 & R \\ 0 & 0 & -R^{\intercal} & M \end{bmatrix}\begin{bmatrix} \mathbf{u}^{n+1} \\ p^{n+1} \\ \mathbf{F}^{n+1} \\ \boldsymbol{\Theta}^{n+1}\end{bmatrix}=\begin{bmatrix} \mathbf{r}+bc_1 \\ bc_2 \\ 0 \\ \mathbf{s}\end{bmatrix}. \tag{18}$$

Now, our objective is to solve the linear system (18) efficiently. In the remainder of this section, we derive the IBPM based on the approach of [16]. To begin with, several augmented operators are first introduced;

$$\tilde{G}=\begin{bmatrix} G & S & 0\end{bmatrix}, \quad \tilde{R}=\begin{bmatrix} 0 & 0 & 0 \\ 0 & 0 & R \\ 0 & -R^{\intercal} & M\end{bmatrix}, \quad \tilde{bc}=\begin{bmatrix} bc_2 \\ 0 \\ \mathbf{s}\end{bmatrix}, \quad \boldsymbol{\Lambda}^{n+1}=\begin{bmatrix} p^{n+1} \\ \mathbf{F}^{n+1} \\ \boldsymbol{\Theta}^{n+1}\end{bmatrix}.$$

Thus, Equation (18) can be written in a compact form as

$$\begin{bmatrix} H & \tilde{G} \\ -\tilde{G}^{\intercal} & \tilde{R}\end{bmatrix}\begin{bmatrix}\mathbf{u}^{n+1} \\ \boldsymbol{\Lambda}^{n+1}\end{bmatrix}=\begin{bmatrix}\mathbf{r}+bc_1 \\ \tilde{bc}\end{bmatrix}. \tag{19}$$

It is realized that p and $\mathbf{F}$ act as the Lagrange multipliers to enforce the fluid incompressibility and the kinematic no-slip boundary condition on the surface, respectively. Subsequently, the block LU decomposition of Equation (19) reads

$$\begin{bmatrix} H & 0 \\ -\tilde{G}^{\intercal} & \tilde{R}+\tilde{G}^{\intercal}H^{-1}\tilde{G}\end{bmatrix}\begin{bmatrix} I & H^{-1}\tilde{G} \\ 0 & I\end{bmatrix}\begin{bmatrix}\mathbf{u}^{n+1} \\ \boldsymbol{\Lambda}^{n+1}\end{bmatrix}=\begin{bmatrix}\mathbf{r}+bc_1 \\ \tilde{bc}\end{bmatrix}$$

In light of the approach by [16], H^{-1} can be approximated by B^N,

$$\begin{bmatrix} H & 0 \\ -\tilde{G}^{\intercal} & \tilde{R}+\tilde{G}^{\intercal}B^N\tilde{G}\end{bmatrix}\begin{bmatrix} I & B^N\tilde{G} \\ 0 & I\end{bmatrix}\begin{bmatrix}\mathbf{u}^{n+1} \\ \boldsymbol{\Lambda}^{n+1}\end{bmatrix}=\begin{bmatrix}\mathbf{r}+bc_1 \\ \tilde{bc}\end{bmatrix}+\begin{bmatrix}\left(HB^N-I\right)\tilde{G}\boldsymbol{\Lambda}^{n+1} \\ 0\end{bmatrix} \tag{20}$$

where B^N is the N-th order Neumann series expansion of H^{-1},

$$H^{-1} \approxeq B^N = \Delta t\left(I + \Delta t \nu L + (\Delta t \nu L)^2 + \cdots + (\Delta t \nu L)^{N-1}\right) = \Delta t \sum_{k=0}^{N-1} (\Delta t \nu L)^k .$$

Let us define $\mathbf{u}^* = \mathbf{u}^{n+1} + B^N \tilde{G} \mathbf{\Lambda}^{n+1}$ as an intermediate velocity. Then, we can rewrite Equation (20) in the following sequential form,

$$\begin{aligned} H\mathbf{u}^* &= \mathbf{r} + bc_1 + \left(HB^N - I\right)\tilde{G}\mathbf{\Lambda}^{n+1}, \\ \left(\tilde{R} + \tilde{G}^\intercal B^N \tilde{G}\right)\mathbf{\Lambda}^{n+1} &= \tilde{G}^\intercal \mathbf{u}^* + \tilde{bc}, \\ \mathbf{u}^{n+1} &= \mathbf{u}^* - B^N \tilde{G}\mathbf{\Lambda}^{n+1}. \end{aligned}$$

We observe that $\mathbf{u}^*$ and $\mathbf{\Lambda}^{n+1}$ can be decoupled by omitting the term $\left(HB^N - I\right)\tilde{G}\mathbf{\Lambda}^{n+1}$ at the righthand side of the momentum equation which results in a fractional step procedure. Hence, the term $\left(HB^N - I\right)\tilde{G}\mathbf{\Lambda}^{n+1}$ is the corresponding splitting error occurring in the momentum equation. It should be noted that the splitting error for the kinematic constraint equations is absent since we are able to preserve $-\tilde{G}^\intercal \mathbf{u}^{n+1} + \tilde{R}\mathbf{\Lambda}^{n+1} = \tilde{bc}$ in Equation (19). By setting $B^N = \Delta t I$ $(N = 1)$, the above scheme becomes

$$\begin{aligned} H\mathbf{u}^* &= \mathbf{r} + bc_1 + \underbrace{(H\Delta t - I)\tilde{G}\mathbf{\Lambda}^{n+1}}_{\text{first-order splitting error}} + O\left(\Delta t^2\right), \\ \left(\frac{1}{\Delta t}\tilde{R} + \tilde{G}^\intercal \tilde{G}\right)\mathbf{\Lambda}^{n+1} &= \frac{1}{\Delta t}\left(\tilde{G}^\intercal \mathbf{u}^* + \tilde{bc}\right), \\ \mathbf{u}^{n+1} &= \mathbf{u}^* - \Delta t \tilde{G}\mathbf{\Lambda}^{n+1}. \end{aligned}$$

The leading first-order splitting error of momentum equation has the form $(H\Delta t - I)\tilde{G}\mathbf{\Lambda}^{n+1} = -\nu\Delta t L\tilde{G}\mathbf{\Lambda}^{n+1}$ due to $H = \frac{1}{\Delta t}I - \nu L$. As in the classical projection method [23,24] for solving the incompressible fluid flows, the first-order splitting error is neglected herein. The first equation involves solving the modified Helmholtz equation for $\mathbf{u}^*$ by using a Fast Fourier Transform (FFT)-based solver. Once $\mathbf{u}^*$ is computed, the remaining goal is to solve the above second equation, i.e., the coupled system of p^{n+1}, $\mathbf{F}^{n+1}$, and $\mathbf{\Theta}^{n+1}$

$$\begin{bmatrix} G^\intercal G & G^\intercal S & 0 \\ S^\intercal G & S^\intercal S & \frac{1}{\Delta t}R \\ 0 & -\frac{1}{\Delta t}R^\intercal & \frac{1}{\Delta t}M \end{bmatrix} \begin{bmatrix} p^{n+1} \\ \mathbf{F}^{n+1} \\ \mathbf{\Theta}^{n+1} \end{bmatrix} = \frac{1}{\Delta t}\begin{bmatrix} G^\intercal \mathbf{u}^* + bc_2 \\ S^\intercal \mathbf{u}^* \\ \mathbf{s} \end{bmatrix}.$$

We first define an intermediate pressure $p^* = p^{n+1} - L^{-1}G^\intercal S\mathbf{F}^{n+1}$. Subsequently, applying the block LU decomposition again yields

$$\begin{aligned} Lp^* &= -\frac{1}{\Delta t}\left(G^\intercal \mathbf{u}^* + bc_2\right), \\ \begin{bmatrix} S^\intercal S + S^\intercal G L^{-1} G^\intercal S & \frac{1}{\Delta t}R \\ -\frac{1}{\Delta t}R^\intercal & \frac{1}{\Delta t}M \end{bmatrix}\begin{bmatrix} \mathbf{F}^{n+1} \\ \mathbf{\Theta}^{n+1} \end{bmatrix} &= \frac{1}{\Delta t}\begin{bmatrix} S^\intercal \mathbf{u}^* \\ \mathbf{s} \end{bmatrix} - \begin{bmatrix} S^\intercal G p^* \\ 0 \end{bmatrix}, \\ p^{n+1} &= p^* + L^{-1}G^\intercal S\mathbf{F}^{n+1}, \end{aligned} \tag{21}$$

where $L \equiv -G^\intercal G$ is the discrete Laplacian operator. It should be noted that, p^{n+1} and $\left[\mathbf{F}^{n+1} \quad \mathbf{\Theta}^{n+1}\right]^\intercal$ are decoupled without compromising the accuracy since the performed block LU decomposition is exact. A constraint equation for the IB force density is derived as

$$S^\intercal\left(S + GL^{-1}G^\intercal S\right)\mathbf{F}^{n+1} + \frac{1}{\Delta t}R\mathbf{\Theta}^{n+1} = S^\intercal\left(\frac{\mathbf{u}^*}{\Delta t} - Gp^*\right)$$

that satisfies the boundary condition at the surface and the kinematic constraint of the fluid-rigid body interaction. The Newton-Euler equations are now solved simultaneously with the constraint equation. It is observed that, in case of the neutrally buoyant rigid body ($\rho_s/\rho_f = 1$ or the operator $M = 0$ in Equation (21)), the translational and angular velocity of the rigid body $\mathbf{\Theta}$ act as the Lagrange multipliers to satisfy the force-free and torque-free constraints of rigid body motion, respectively. That is, $-R^\intercal \mathbf{F}^{n+1} = \mathbf{s}$ or precisely,

$$\begin{aligned} &\sum_{k=1}^{K} \mathbf{F}_k^{n+1} \Delta A(\mathbf{X}_k^n) = 0, \\ &\sum_{k=1}^{K} \mathbf{\Gamma}_k^0 \times Q^\intercal \mathbf{F}_k^{n+1} \Delta A(\mathbf{X}_k^n) = 0. \end{aligned}$$

The numerical stability is not violated as the linear system in Equation (21) remains non-singular when the operator $M = 0$. Hence the present method is capable of computing a moderate range of density ratios including the unity without any modification. On the other hand, the method in [12] is unstable for the neutrally buoyant rigid body case due to the singularity of the inertial matrix. Although a modified Poisson system was proposed to circumvent this issue, it was not practically implemented therein.

For convenience, the numerical algorithm of the IBPM for solving the fluid-rigid body interaction problem is summarized in Algorithm 1. We also analyze the computational efficiency for each computation step in Algorithm 1. For the current implementation, the discrete Laplacian operator L and discrete modified Helmholtz operator H are diagonalizable in Fourier space. We, therefore, do not explicitly construct the inversion of H and L but applying the FFT-based modified Helmholtz and Poisson solvers directly to compute the intermediate velocity $\mathbf{u}^*$, intermediate pressure p^* and pressure p^{n+1} in Line 4, Line 5, and Line 7, respectively. In Line 6, we apply the GMRES iterative solver [25] to solve the coupled system of equations for $\mathbf{F}^{n+1}$ and $\boldsymbol{\Theta}^{n+1}$. Each GMRES iteration requires applying one FFT-based Poisson solver using a reverse communication mechanism and sparse matrix-vector products. The rigid body has at most six degrees of freedom in 3D, and the size of the sparse matrix-vector product is proportional to the number of Lagrangian markers, which is one dimension lower than the Eulerian grid number. Hence the computational cost is dominated by the number of the FFT-based Poisson solver applied. In practice, an average number of 1-5 GMRES iterations is required to converge to the prescribed error tolerance of order h^2. Once the pressure p^{n+1} and force density $\mathbf{F}^{n+1}$ are available, we update the intermediate velocity $\mathbf{u}^*$ at Line 8 to the velocity $\mathbf{u}^{n+1}$ that satisfy both the discrete fluid incompressibility and discrete kinematic no-slip boundary condition on the surface. Note that, the present velocity interpolation and boundary force spreading operators are all time-lagged in the discrete delta function computations so that an $O(\Delta t)$ error is introduced to the boundary condition. Instead of using the interpolation formula to compute the surface velocity and updating the surface position vector $\mathbf{X}^{n+1}$, we adopt the principle of rigid body dynamics as in [26]. In Line 9, the position vector of the rigid body's center of mass $\mathbf{X}_c^{n+1}$ is computed once the translational velocity $\mathbf{U}_c^{n+1}$ is obtained. Then, in Line 10, we evaluate the unit quaternion $\mathbf{q}^{n+1}$ by performing time integration on W^{n+1} and $\left|\boldsymbol{\omega}_c^{n+1}\right|$ as derived in Equation (13). At last, we compute the matrix Q and update the position vector $\mathbf{X}^{n+1}$ of the rigid body in Line 11. At this point, one can evaluate the angular velocity in the inertial frame $\bar{\boldsymbol{\omega}}_c^{n+1} = Q\boldsymbol{\omega}_c^{n+1}$. Clearly, Line 8 to Line 11 are just variable substitutions, so the overall computational cost is dictated by the cost of the total number of FFT-based fast solvers applied.

Algorithm 1: IBPM for fluid-rigid body interaction problem.

1 Initialize Eulerian variables $\mathbf{u}^0$, p^0.
2 Initialize Lagrangian variables $\mathbf{X}_c^0$, $\mathbf{X}^0$, $\mathbf{F}^0$, $\boldsymbol{\Theta}^0 = [\mathbf{U}_c^0 \quad \boldsymbol{\omega}_c^0]^T$.
3 **while** $t^{n+1} \le T_{final}$ **do**
4 Solve $H\mathbf{u}^* = \mathbf{r} + bc_1$ with FFT-based modified Helmholtz solver.
5 Solve $Lp^* = -\frac{1}{\Delta t}\left(G^\intercal \mathbf{u}^* + bc_2\right)$ with FFT-based Poisson solver.
6 Solve $\begin{bmatrix} S^\intercal S + S^\intercal G L^{-1} G^\intercal S & \frac{1}{\Delta t}R \\ -\frac{1}{\Delta t}R^\intercal & \frac{1}{\Delta t}M \end{bmatrix}\begin{bmatrix} \mathbf{F}^{n+1} \\ \boldsymbol{\Theta}^{n+1} \end{bmatrix} = \frac{1}{\Delta t}\begin{bmatrix} S^\intercal \mathbf{u}^* \\ \mathbf{s} \end{bmatrix} - \begin{bmatrix} S^\intercal G p^* \\ 0 \end{bmatrix}$ with GMRES. At each iteration, FFT-based Poisson solver is applied using reverse communication mechanism.
7 Solve $p^{n+1} = p^* + L^{-1} G^\intercal S \mathbf{F}^{n+1}$ with FFT-based Poisson solver.
8 Compute $\mathbf{u}^{n+1} = \mathbf{u}^* - \Delta t\left(Gp^{n+1} + S\mathbf{F}^{n+1}\right)$.
9 Compute $\mathbf{X}_c^{n+1} = \mathbf{X}_c^n + \Delta t\left(\mathbf{U}_c^{n+1} - \mathbf{U}_c^n\right)$.
10 Compute $\mathbf{q}^{n+1} = \left[\cos\left(\left|\boldsymbol{\omega}_c^{n+1}\right|\Delta t/2\right)\mathbf{I} + \frac{2}{\left|\boldsymbol{\omega}_c^{n+1}\right|}\sin\left(\left|\boldsymbol{\omega}_c^{n+1}\right|\Delta t/2\right)W^{n+1}\right]\mathbf{q}^n$, and then Q by Eq. (11).
11 Compute $\mathbf{X}_k^{n+1} = \mathbf{X}_c^{n+1} + Q\boldsymbol{\Gamma}_k^0, \quad \forall k$.
12 **end**

The present IBPM holds a key feature such that both the discrete fluid incompressibility and discrete kinematic no-slip boundary condition on the rigid body surface are satisfied simultaneously at every time step, i.e., $-G^\intercal \mathbf{u}^{n+1} = bc_2$ in Equation (15) and $-S^\intercal \mathbf{u}^{n+1} = -R^\intercal \boldsymbol{\Theta}^{n+1}$ in Equation (16). For completeness, we state the proof as follows. By applying the discrete divergence operator $-G^\intercal$ on $\mathbf{u}^{n+1}$ in Line 8 of Algorithm 1 yields

$$
\begin{aligned}
&-G^\intercal \mathbf{u}^{n+1} \\
=&-G^\intercal \mathbf{u}^* + \Delta t\left(G^\intercal G p^* + G^\intercal S\mathbf{F}^{n+1}\right) \\
=&\Delta t L p^* + bc_2 + \Delta t\left(G^\intercal G p^{n+1} + G^\intercal S\mathbf{F}^{n+1}\right) \quad \text{by Line 5} \\
=&-\Delta t\left(G^\intercal G p^{n+1} + G^\intercal S\mathbf{F}^{n+1}\right) + bc_2 + \Delta t\left(G^\intercal G p^{n+1} + G^\intercal S\mathbf{F}^{n+1}\right) \quad \text{by } L \equiv -G^\intercal G \text{ and Line 7} \\
=&bc_2.
\end{aligned}
$$

Hence, the discrete fluid incompressibility is satisfied. In a similar manner, by applying the interpolation operator $-S^\intercal$ on $\mathbf{u}^{n+1}$ in Line 8 of Algorithm 1 yields

$$
\begin{aligned}
& - S^{\top}\mathbf{u}^{n+1} \\
&= - S^{\top}\mathbf{u}^{*} + \Delta t\left(S^{\top}Gp^{n+1} + S^{\top}S\mathbf{F}^{n+1}\right) \\
&= - \Delta t\left(S^{\top}Gp^{*} + S^{\top}GL^{-1}GS\mathbf{F}^{n+1} + S^{\top}S\mathbf{F}^{n+1}\right) - R\boldsymbol{\Theta}^{n+1} + \Delta t\left(S^{\top}Gp^{n+1} + S^{\top}S\mathbf{F}^{n+1}\right) \quad \text{by Line (6)} \\
&= - \Delta t\left(S^{\top}Gp^{n+1} - S^{\top}GL^{-1}GS\mathbf{F}^{n+1} + S^{\top}GL^{-1}GS\mathbf{F}^{n+1}\right) - R\boldsymbol{\Theta}^{n+1} + \Delta t\left(S^{\top}Gp^{n+1}\right) \quad \text{by Line (7)} \\
&= - R\boldsymbol{\Theta}^{n+1}.
\end{aligned}
$$

Hence, the discrete kinematic no-slip boundary condition on the body surface is also satisfied.

We conclude this section by summarizing the differences and novelty of the present Algorithm 1 comparing to the previous similar work in [12] as follows.

- At the prediction step, we solve the fluid velocity $\mathbf{u}^*$ (Line 4) and the pressure p^* (Line 5) sequentially while in [12], the authors solve the fluid velocity and rigid body velocities (the translational velocity $\mathbf{U}_c$ and angular velocity $\boldsymbol{\omega}_c$) altogether. So in our prediction step, FFT-based fast modified Helmholtz and Poisson solvers can be efficiently applied to find $\mathbf{u}^*$ and p^*, respectively. Thus, our prediction step remains identical to the original pressure projection method for the incompressible Navier-Stokes equations. In Line 6, we directly solve the Newton-Euler equations for the rigid body velocities without the prediction step to ensure the discrete fluid incompressibility and discrete kinematic no-slip boundary condition on the body surface at every time step, i.e., $-G^{\top}\mathbf{u}^{n+1} = bc_2$ and $-S^{\top}\mathbf{u}^{n+1} = -R^{\top}\boldsymbol{\Theta}^{n+1}$.
- In Line 6, the immersed boundary force density $\mathbf{F}^{n+1}$ and the rigid body velocities $\boldsymbol{\Theta}^{n+1}$ are solved in a coupled linear system while in [12], the IB force density and the pressure are solved together instead. One can immediately see the size of the present linear system is significantly smaller than the one used in [12]. Precisely speaking, in 3D case, the number of unknowns in present linear system is $3K + 6$, while the number of unknowns in the linear system in [12] is $3K + N^3$; here, K denotes the number of Lagrangian markers and $N = N_x = N_y = N_z$ denotes the grid number used in each coordinate direction. In addition, the present linear system in Line 6 can be solved via GMRES iterative method while each GMRES iteration requires applying one FFT-based Poisson solver using a reverse communication mechanism and sparse matrix-vector products.
- We apply the present IBPM to fluid-rigid body interaction problems using 2D and 3D spherical and spheroidal rigid bodies (see Section 5), while in [12] the rigid body is a 2D circular cylinder. Certainly, we believe that the proposed method in [12] can be applied to 3D different geometries too. However, from the authors' point of view, 3D fluid-rigid body interaction problem is significantly more complex than its 2D counterpart, and the extension is non-trivial. For instance, in the present study, we employ an orthogonal rotation matrix represented by a unit quaternion in 3D fluid-rigid body interaction problems which is not needed in 2D case. By introducing such rotation matrix, the dynamics of 3D rigid bodies of arbitrary geometry can be computed efficiently.

5. Numerical results

5.1. Grid convergence study for the Navier-Stokes solver

First, we perform a grid convergence study for the present Navier-Stokes solver using a fully three-dimensional analytic solution based on the generalized Beltrami flows [27], i.e.

$$
\begin{aligned}
u_{\text{exact}} = \frac{4\sqrt{2}}{3\sqrt{3}} \Big\{ & [a\cos(kx) + b\sin(kx)][-c\sin(ky) + d\cos(ky)][e\cos(kz) + f\sin(kz)] \\
& - [-a\sin(kz) + b\cos(kz)][c\cos(kx) + d\sin(kx)][e\cos(ky) + f\sin(ky)] \Big\} e^{3\nu k^2 t} u_0,
\end{aligned}
$$

$$
\begin{aligned}
v_{\text{exact}} = \frac{4\sqrt{2}}{3\sqrt{3}} \Big\{ & [a\cos(ky) + b\sin(k)][-c\sin(kz) + d\cos(kz)][e\cos(kx) + f\sin(kx)] \\
& - [-a\sin(kx) + b\cos(kx)][c\cos(ky) + d\sin(ky)][e\cos(kz) + f\sin(kz)] \Big\} e^{3\nu k^2 t} v_0,
\end{aligned}
$$

$$
\begin{aligned}
w_{\text{exact}} = \frac{4\sqrt{2}}{3\sqrt{3}} \Big\{ & [a\cos(kz) + b\sin(kz)][-c\sin(kx) + d\cos(kx)][e\cos(ky) + f\sin(ky)] \\
& - [-a\sin(ky) + b\cos(ky)][c\cos(kz) + d\sin(kz)][e\cos(kx) + f\sin(kx)] \Big\} e^{3\nu k^2 t} w_0,
\end{aligned}
$$

where

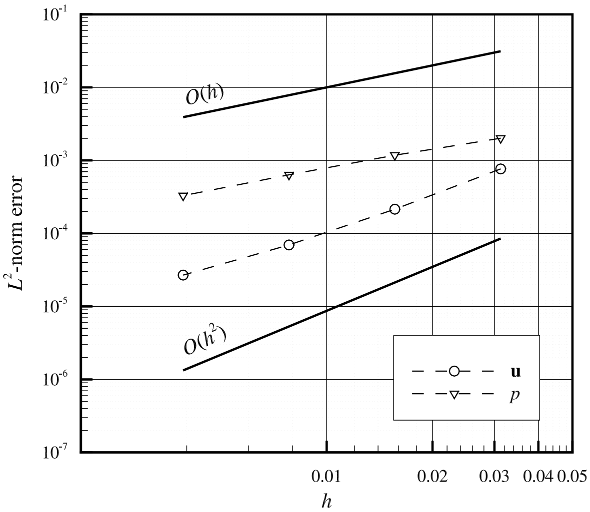

Fig. 2. Grid refinement analysis of fluid solution variables, i.e. the velocity $\mathbf{u}$ and pressure p for the Navier-Stokes solver.

$$a = -\frac{\sqrt{3}+R}{2\sqrt{1+R^2}}, \quad b = \frac{1-\sqrt{3}R}{2\sqrt{1+R^2}}, \quad c = \frac{\sqrt{3}-R}{2\sqrt{1+R^2}}$$
$$d = \frac{1+\sqrt{3}R}{2\sqrt{1+R^2}}, \quad e = \frac{1}{\sqrt{1+R^2}}, \quad f = \frac{R}{\sqrt{1+R^2}}.$$

Here, $R = 1/\sqrt{3}$, k is the wavenumber, $L = 2\pi/k$ is the wavelength, and u_0, v_0, w_0 are the reference velocity components. Note that all the velocity components depend non-trivially on all three Cartesian coordinate directions. In the present study, we set $u_0 = v_0 = w_0 = 1$, $L = 1$ and define the periodic fluid domain $\Omega_f = [0,1] \times [0,1] \times [0,1]$. For a linear refinement, a time step of $\Delta t = h$ is employed in conjunction with a series of grid resolution $h = 1/32, 1/64, 1/128, 1/256$. All the simulations are time-marched from $t = 0$ to $t = 1.0$. To quantify the grid convergence rate of the solution variables, the normalized L^2-norm errors are evaluated by taking the difference between the numerical solutions and analytic solution. Fig. 2 shows the grid refinement analysis of the Eulerian variables, i.e., the fluid velocity $\mathbf{u}$, and pressure p. The numerical results indicate that the velocity and the pressure both exhibit first-order convergence rate in L^2-norm as h decreases.

5.2. Grid convergence study for the immersed boundary projection method

We conduct a grid convergence study for the IBPM by simulating the sedimentation of a 3D oblate spheroid in a quiescent fluid. The shape of the oblate spheroid is parameterized by $\mathbf{X}(\alpha,\beta) = (a\cos\alpha\sin\beta, b\sin\alpha\sin\beta, b\cos\beta)$, with $a < b$. The aspect ratio of the oblate spheroid is defined as $a_r = b/a = \left(1+\sqrt{5}\right)/2$. Given an equivalent spherical diameter $D = \sqrt[3]{6V_s/\pi} = 1$, the oblate spheroid is initially placed in a quiescent fluid domain $\Omega_f = [-2D, 2D] \times [-2D, 2D] \times [-2D, 2D]$ with periodic boundary condition at all directions, and inclined at angle $\mathbf{\Phi} = (-\pi/4, -\pi/4, -\pi/4)$. A time step of $\Delta t = h/4$ is employed in conjunction with a linear refinement of grid resolution $h = D/16, D/32, D/64, D/128$. Referring to Fig. 3, the mesh of the oblate spheroid is defined by a linear transformation applied to the mesh of a sphere which is created by successive geodesic subdivisions from a dodecahedron, i.e. dividing pentagons into triangles with a center point. In practice, the size of the Lagrangian mesh should be chosen as $\Delta A \approx O(h^2)$. The number of markers is therefore inversely proportional to the mesh width. According to the numerical experiments, the optimal ratio of ΔA to h^2 is found to be ranging from 1/2 to 2 in order to maintain the desired accuracy and robustness of the IBPM. A higher ratio will cause fluid leakage across the immersed boundary, whereas a smaller ratio will degrade the robustness and increase the number of iterations of GMRES required to converge to a prescribed tolerance, thus increasing the total computation time. The density ratio is set as $R_\rho = \rho_s/\rho_f = \left(1+\sqrt{5}\right)/2$ with $\rho_f = 1$, and the gravitational acceleration is set as $\mathbf{g} = (0, -1, 0)$. The stopping tolerance of GMRES is set to be h^2. All the simulations are time-marching from $t = 0$ to $t = 1.0$. The average number of GMRES iteration with tolerance h^2 is maintained at 1 to 4 iterations for all the grid resolutions, which is essentially grid-independent. The numerical solution of a fine grid resolution $h = D/256$ is taken as the reference solution since the analytical solution is not available. The grid convergence rate of the solution variables is quantified using the normalized L^2-norm errors evaluated by taking the difference between the numerical solutions and interpolated reference solutions. Fig. 4 shows the grid refinement analysis of the velocity $\mathbf{u}$, pressure p, and IB force density $\mathbf{F}$. The numerical results indicate that both the Eulerian and Lagrangian variables exhibit an average of first-order convergence rate in L^2-norm. Nevertheless, a slightly better accuracy than formally first-order is observed at finer grid resolution primarily due to the adoption of the interpolated numerical

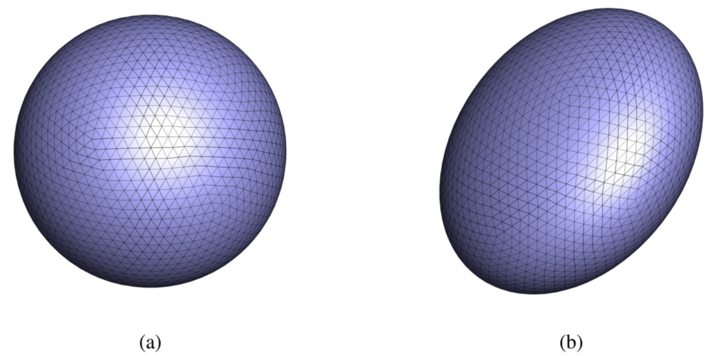

Fig. 3. (a) A mesh of a sphere created by successive geodesic subdivisions from a dodecahedron. (b) A mesh of an oblate spheroid created by a linear transformation applied to the mesh of a sphere.

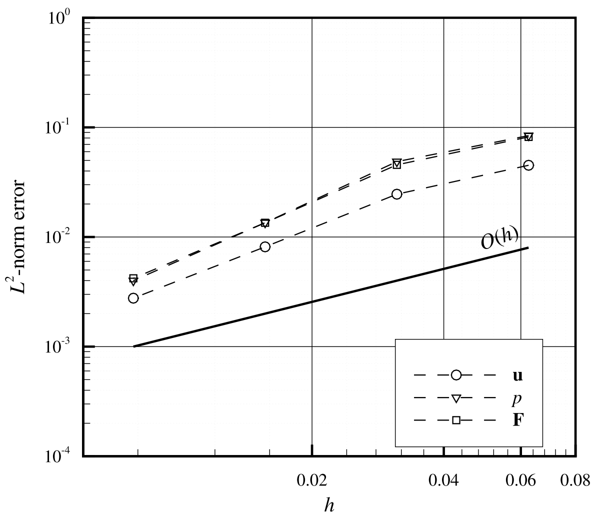

Fig. 4. Grid refinement analysis of the velocity **u**, pressure p, and force density **F** for the IBPM.

solution from the finest mesh as the reference solution since the analytical solution is not available. This practice inevitably causes certain deviations, and should be perceived in the present convergence study.

5.3. Neutrally buoyant circular cylinder in a shear flow

We consider the dynamics of a neutrally buoyant 2D circular cylinder $M_e = I_e = 0$ with diameter D in a shear flow $\mathbf{u} = (\gamma y/L, 0)$. Note that in 2D, I_e is simply a scalar representing the moment of inertia about the z-axis. The circular cylinder is initially placed in a channel with a height of $L = 4D$ and at an offset of D vertically from the centerline of the channel. Following the previous work [12], the Reynolds number based on the shear rate is $Re_\gamma = \gamma L^2/\nu = 40$. Under the prescribed condition, the cylinder rotates and migrates from the initial position to the centerline of the channel. The cylinder eventually settles its position at the centerline and continues to rotate at a constant rate of 0.47γ approximately. We time-march the simulation from $\gamma t = 0$ to $\gamma t = 256$ using a mesh size of $h = D/32$ with $D = 1$ and a time step of $\Delta t = h/L$. The average number of GMRES iteration is 2.16 in this case.

Fig. 5 shows the comparison between the present study and the numerical solution of [12]. Both the transient profile of the vertical displacement y/L and angular velocity in the inertial frame $\bar{\omega}_z/\gamma$ are in excellent agreement with the numerical solution of [12]. In contrast to the previous studies, the present method eliminates the oscillation in the migration trajectory observed in the previous studies. This oscillating behavior in the IB simulation of fluid-rigid body was referred to as 'grid locking' [28]. As a concluding remark, the present method shows the ability to efficiently and stably solve the fluid-rigid body interaction problem for a neutrally buoyant rigid body without any ad hoc numerical modification.

5.4. Sedimentation of an elliptic cylinder

We consider a 2D elliptic cylinder falling under gravity force in a rectangular domain filled with quiescent fluid. The minor and major axes of the elliptic cylinder are set as D and $2D$, respectively. The width of the rectangular domain is

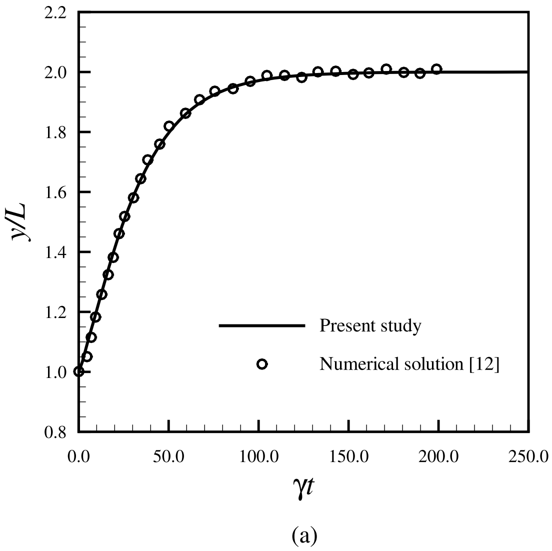

Fig. 5. Numerical solution of a neutrally buoyant circular cylinder in a shear flow compared to the previous study of [12]. (a) Vertical displacement y/L. (b) Angular velocity $\bar{\omega}_z/\gamma$.

$L = 8D$, and the height is $20L$. Here, as in [29,30], we use the fixed side walls for which the homogeneous Dirichlet boundary condition is imposed for the velocity while the homogeneous Neumann boundary condition is imposed for the pressure in the Navier-Stokes equations. Given the density ratio of the solid cylinder to the fluid $R_\rho = \rho_s/\rho_f$, the corresponding mass and inertia are $M_s = R_\rho \rho_f(\pi D^2/2)$ and $I_s = 5M_s D^2/4$, respectively. Note that in 2D, I_s is simply a scalar representing the moment of inertia about the z-axis.

Following the previous works [29,30], three cases of different density ratio are considered, i.e. $R_\rho = 1.01,\ 1.1,\ 1.5$ with the corresponding Galileo number $Ga = 10,\ 30,\ 70$, where $Ga := \sqrt{|R_\rho - 1||\mathbf{g}|D^3}/\nu$. The elliptic cylinder is initially positioned at $x = L/2$ and $y = 15L$, inclined at angle $\phi_z = -\pi/4$. Given the time $\lambda_t = \sqrt{D/|\mathbf{g}|}$, we time-march the simulation using a mesh size of $h = D/16$ with $D = 1$ and a time step of $\Delta t = \lambda_t h/L$. The sedimentation of the elliptic cylinder of three different density ratios R_ρ with $\rho_f = 1$ is simulated starting from its prescribed initial position until it reached the bottom surface. The corresponding average number of the GMRES iteration for the simulations are 1.1, 1.3, 2.2, respectively.

Fig. 6 shows the snapshots of the sedimentation of an elliptic cylinder from the position $y = 10L$ to $y = 15L$ for (a) $R_\rho = 1.01$, (b) $R_\rho = 1.1$, (c) $R_\rho = 1.5$. Fig. 7(a) and (c) shows the comparison between the present numerical solutions and the numerical results of [30] based on IB-lattice Boltzmann method. Fig. 7(b) shows the comparison between the present numerical solution and the numerical solution of [29] based on the finite element method. As shown in Fig. 6, all the elliptic cylinders tremendously rotate and drift away from their initial position right after released from their initial position and angle. Subsequently, the elliptic cylinders with $R_\rho = 1.01$ and $R_\rho = 1.1$ are gradually orientating their major axis normal to the direction of gravity force and migrating toward the initial horizontal position $x = L/2$ while descending to the bottom surface of the domain. Referring to Fig. 7 (a)-(d), the trajectory of the elliptic cylinder with $R_\rho = 1.1$ exhibits a small amplitude in contrast to the elliptic cylinder with $R_\rho = 1.01$. As shown in Fig. 7 (e)-(f), the elliptic cylinder with $R_\rho = 1.5$ shows a large amplitude of zig-zag motion on the contrary, while descending to the bottom surface. This behavior is attributed to the fluctuating drag forces acting on the cylinder. The present numerical solutions show an excellent agreement with the numerical solutions from the literature. The present method correctly captures the flow physics of the sedimentation of the elliptic cylinder of different density ratios, including the one close to unity which poses a challenge in the previous numerical studies.

5.5. *Sedimentation of a sphere*

We consider the sedimentation of a 3D sphere falling under gravity in a rectangular domain filled with quiescent fluid. The diameter of the sphere is D. The height of the rectangular domain is $L = 10D$, while the width and length of the rectangular domain is $(2/3)L$. Given the density ratio of the sphere to the fluid $R_\rho = \rho_s/\rho_f$, the corresponding mass and inertia are $M_s = R_\rho \rho_f(\pi D^3/6)$ and $\mathbf{I}_s = M_s D^2/10\mathbf{I}$, respectively, where $\mathbf{I}$ is the identity matrix.

Following the previous experimental work [31] using a particle image velocimetry system, three cases of different density ratio are considered, i.e. $R_\rho = 1.155,\ 1.164,\ 1.167$ with the corresponding Galileo number $Ga = 5.88,\ 19.85,\ 38.87$. Initially, the sphere is positioned at $y = 8D$ from the bottom surface. We time-march the simulation using a mesh size of $h = 5D/96$ with $D = 1$ and a time step of $\Delta t = h/4D$. The sedimentation of the sphere of three different density ratios R_ρ with $\rho_f = 1$

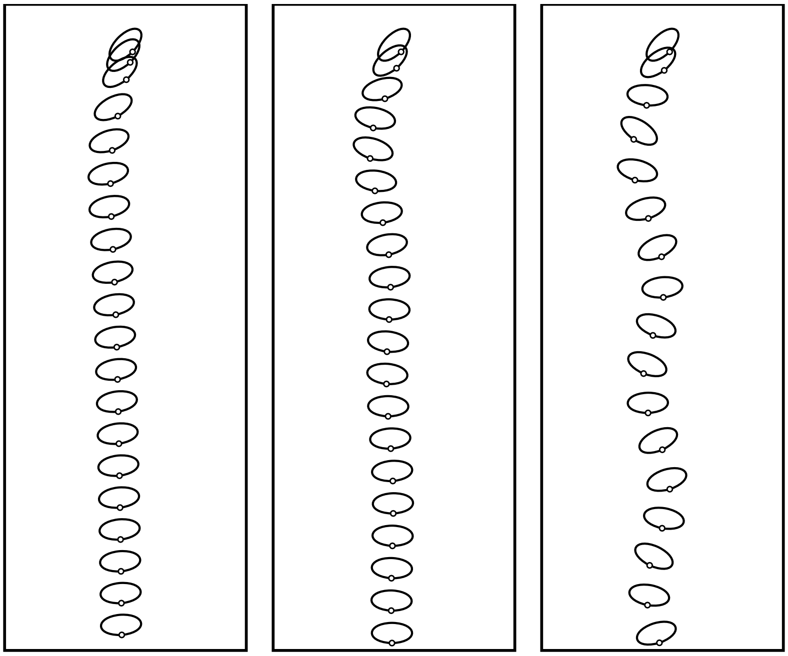

Fig. 6. Snapshots of the sedimentation of an elliptic cylinder from $y = 10L$ to $y = 15L$. (a) $R_\rho = 1.01$, (b) $R_\rho = 1.1$, (c) $R_\rho = 1.5$. A marker is used to track the orientation of the elliptic cylinder.

is computed starting from its prescribed initial position until it reached the bottom surface. The corresponding average number of the GMRES iteration for the simulations are 1.3, 1.1, 4.3, respectively.

Fig. 8(a) shows the vertical trajectory of the sphere with respect to time. The present numerical results agree well with the experimental results for all three cases. Fig. 8(b) shows the falling normalized vertical velocity of the sphere with respect to time. We observe a slight discrepancy between the present numerical results and experimental results in terms of maximum terminal velocity. Nevertheless, the present numerical results show that the acceleration and deceleration profiles are captured correctly for all three cases.

5.6. Neutrally buoyant ellipsoid in a shear flow

We consider the dynamics of a neutrally buoyant 3D prolate spheroid $M_e = 0, \mathbf{I}_e = \mathbf{0}$ in a planar shear flow $\mathbf{u} = (\gamma(y/L - 1/2), 0, 0)$. The prolate spheroid is parameterized by $\mathbf{X}(\alpha, \beta) = (a\cos\alpha\sin\beta, b\sin\alpha\sin\beta, a\cos\beta)$, with $a < b$. The aspect ratio is defined as $a_r = b/a = \left(1+\sqrt{5}\right)/2$. Given an equivalent spherical diameter $D = \sqrt[3]{6V_s/\pi} = 1$, the computational domain's length, width, and height are set as $L = 8D$. The spheroid is initially placed at the center of the domain with zero translational and angular velocity. The initial orientation is set as $\Phi = (0, -\pi/4, 0)$. The Reynolds number based on the shear rate is $Re_\gamma = \gamma D^2/\nu = 1$. We time-march the simulation from $\gamma t = -2$ to $\gamma t = 256$ using a mesh size of $h = D/32$ and a time step of $\Delta t = h/L$. In order to minimize the error caused by abrupt start, the spheroid is fixed from $\gamma t = -2$ to $\gamma t = 0$, and a slowly increasing shear flow $\mathbf{u} = (\gamma(y/L - 1/2)\sin(\pi(\gamma t + 2)/4), 0, 0)$ is imposed. Afterward, the spheroid is free to move from $\gamma t = 0$ to $\gamma t = 256$. The average number of GMRES iteration for the simulation is 3.9.

Fig. 9 depicts the transient profiles of the prolate spheroid in the planar shear flow from $\gamma t = 1$ to $\gamma t = 16$. The prolate spheroid tumbles in the flow-gradient plane periodically and is constrained to rotation in the shear plane. The distribution of the normalized surface shear stress magnitude is also depicted in the figure by contour plots. One can observe that, the higher values occur at the surface normal to the flow direction. In addition, the maximum shear stress is observed to be varying with time due to the varying orientation angle while the minimum shear stress always occurs at the center of rotation. Fig. 10 compares the present numerical results with Jeffery's analytical solution [32] in terms of angular velocity in the inertial frame about z-axis $\bar{\omega}_z$ and the corresponding orientation of the ellipsoid ϕ_z with respect to time. The analytical solution [32] is given by

$$\tan\phi_z = a_r \tan\left(\frac{2\pi t}{T} + \phi_{0,z}\right), \quad T = \frac{2\pi\left(a_r + a_r^{-1}\right)}{\gamma},$$
$$\bar{\omega}_z = \frac{\gamma}{a^2 + b^2}\left(b^2\cos^2\phi_z + a^2\sin^2\phi_z\right),$$

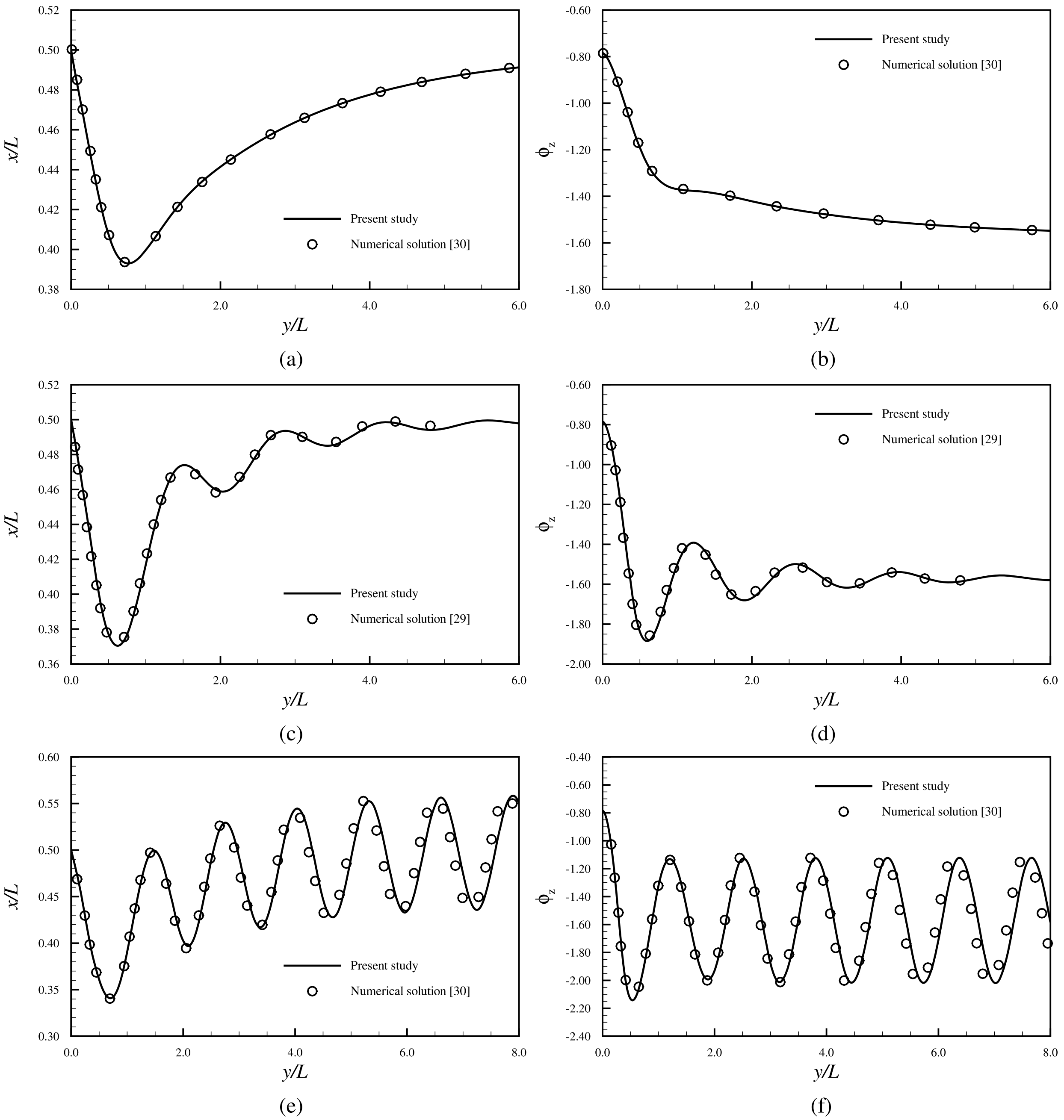

Fig. 7. Numerical solution of the sedimentation of an ellipse cylinder compared to the previous numerical solutions [29,30]. (a), (c), (e) are the trajectory of the ellipse cylinder with $R_\rho = 1.01$, $R_\rho = 1.1$, $R_\rho = 1.5$, respectively. (b), (d), (f) are the orientation angle for the cases $R_\rho = 1.01$, $R_\rho = 1.1$, $R_\rho = 1.5$, respectively.

where $\phi_{0,z}$ is the initial orientation of the ellipsoid. Clearly from the analytical solution, the specific ellipsoid orbit depends on the shear rate, its aspect ratio, and initial orientation. The present numerical results and the theoretical solutions are in excellent agreement, hence validating the present method in resolving the tumbling motion of the ellipsoid.

6. Conclusion

In the present study, we have developed an immersed boundary projection method (IBPM) for solving the coupled Naiver-Stokes and Newton-Euler equations to simulate the fluid-rigid body interaction problems in 2D and 3D, applicable to different geometries and density ratios. We solve the Naiver-Stokes equations in the inertial frame, while for the rigid body dynamics, we solve translational velocity in the inertial frame and angular velocity in the non-inertial frame. Thus the

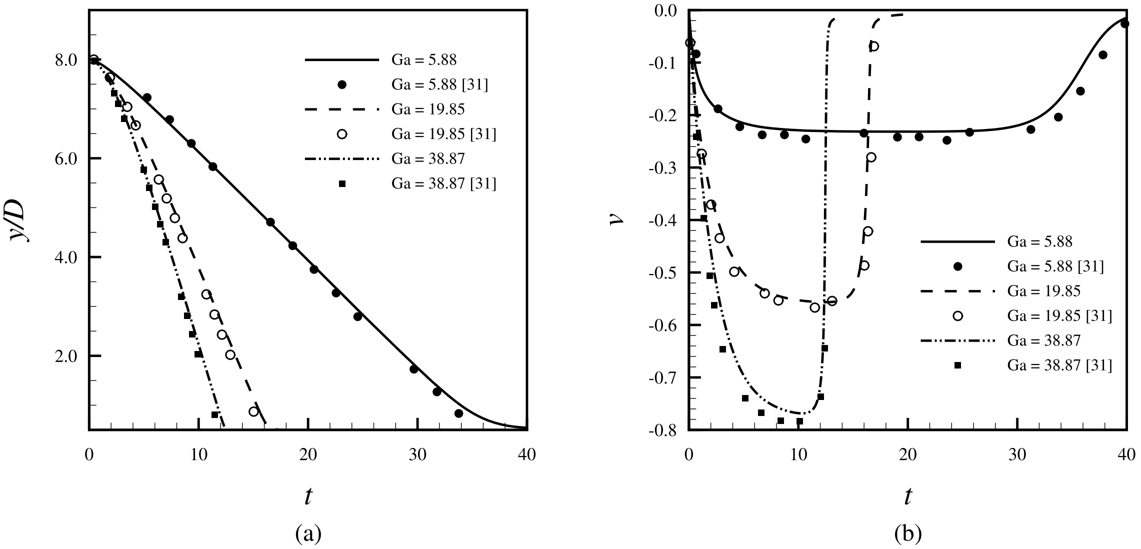

Fig. 8. Numerical solution of the sedimentation of a sphere compared to the experimental data of [31]. (a) Vertical trajectory of the sphere with respect to time. (b) Falling vertical velocity of the sphere with respect to time.

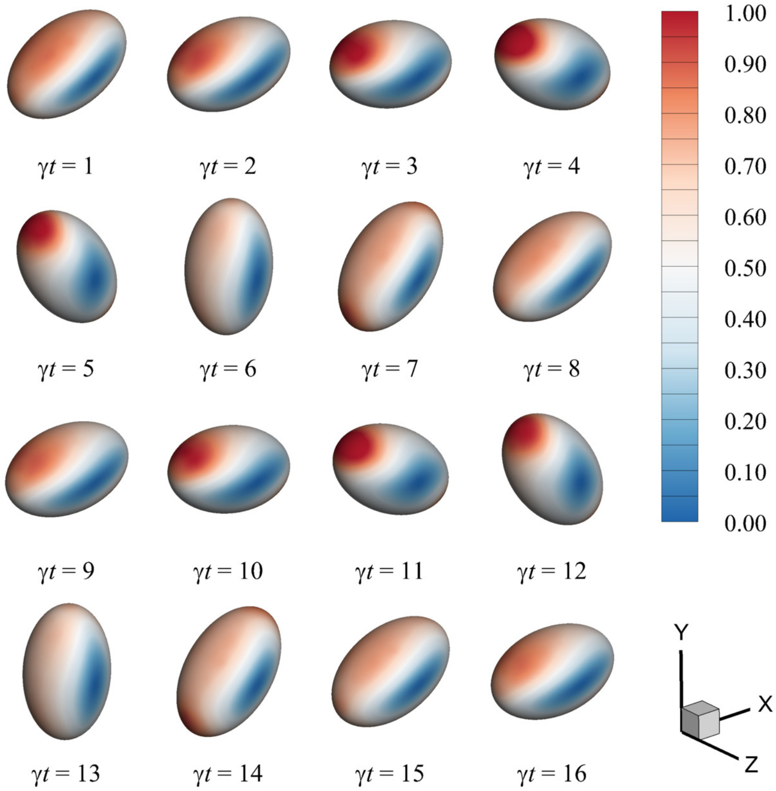

Fig. 9. Transient profiles of the prolate spheroid tumbles in the planar shear flow from $\gamma t = 1$ to $\gamma t = 16$. The contour levels are representing the distribution of the normalized surface shear stress magnitude.

time derivative of the moment of inertia tensor can be eliminated in this case. Rotating the vector in the non-inertial frame to the inertial frame or vice versa can be done using an orthogonal rotation matrix represented by the unit quaternion. Applying the transformed force density, the governing equations can be cast in a block skew-symmetric algebraic form.

By utilizing the fractional step analysis of the IB formulation [16], we have exploited the algebraic structure of the underlying scheme and applied the block LU decomposition technique to develop the numerical algorithm. As a result, all the Eulerian variables are decoupled while maintaining numerical stability and accuracy, which allows us to solve each of

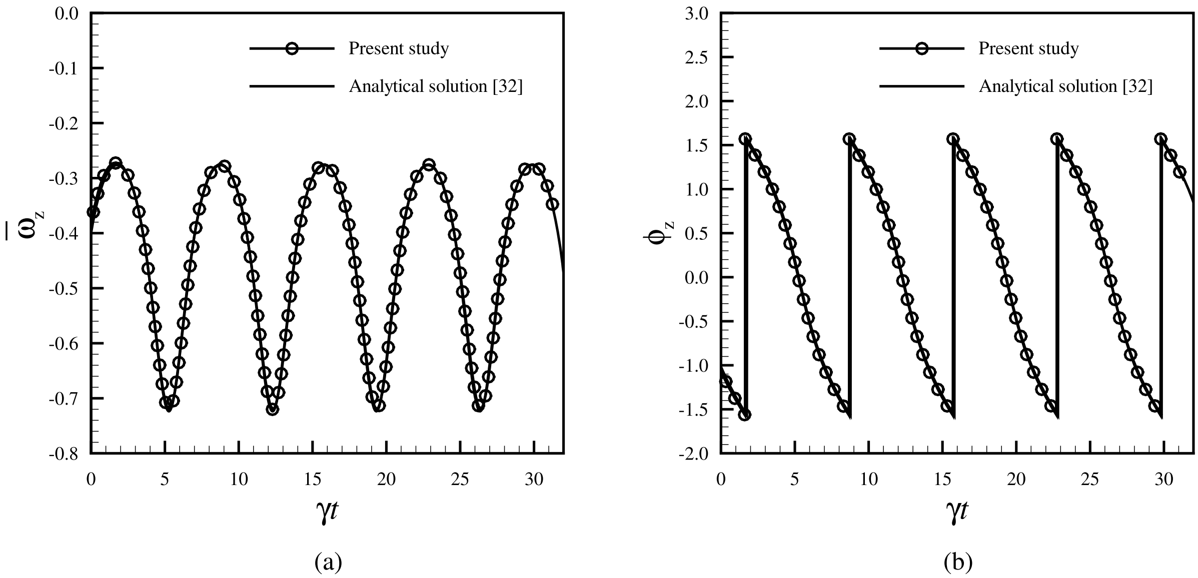

Fig. 10. Comparison between the present numerical solution and analytical solution [32]. (a) Angular velocity $\bar{\omega}_z$. (b) Orientation angle ϕ_z.

the Eulerian variables independently. Furthermore, the Newton-Euler equations are coupled with the constraint equation of the IB force density. Nevertheless, the coupled system can be solved with ease since the rigid body has at most six degrees of freedom in 3D, and the number of Lagrangian markers is one dimension lower than the Eulerian grid number.

The key feature of the present IBPM lies in its computational efficiency. The governing equations can be decomposed into several sub-equations and then solved sequentially in a single time step. At the same time, both the discrete fluid incompressibility and discrete kinematic no-slip boundary condition can be satisfied simultaneously. For the present implementation, we utilize the FFT-based Poisson and modified Helmholtz solvers to compute the inverse of the Laplacian and modified Helmholtz operators, respectively. The coupled system for the IB force density and rigid body velocities is computed iteratively using the GMRES method. Each GMRES iteration requires only to call a FFT-based solver once and sparse matrix-vector products. In addition, the numerical results have shown that the average number of GMRES iteration is between 1 to 5. In contrast to the conventional IB formulation, numerical stability is maintained naturally in the present method for a moderate range of density ratios including unity without any ad hoc modification, which is the primary stability issue in the previous studies [3,12] of the immersed boundary method. The present IBPM can deal with a larger density ratio since the IBPM is derived carefully from the implicit discretization of the coupled Navier-Stokes and Newton-Euler system. Note that the rigid body dynamics will dictate the system in case of a large density ratio. Therefore, the time step (CFL condition) will be restricted by the rigid body dynamics rather than the fluid flows.

We have demonstrated the accuracy and robustness of the present algorithm by solving the fluid-rigid body interaction problems in 2D and 3D involving spherical and spheroidal rigid bodies with a moderate range of density ratios. The numerical results are agreed well with the analytical and previous numerical results from the literature. Moreover, the computational framework provides excellent versatility in the implementation and future extension. We envision a long term study utilizing IBPM to simulate more physically complex fluid-rigid body interaction dynamics, including conjugate heat transfer, electrohydrodynamics and magnetohydrodynamics.

CRediT authorship contribution statement

Kian Chuan Ong: Conceptualization, Methodology, Project administration, Software, Validation, Writing – original draft, Writing – review & editing. **Yunchang Seol:** Conceptualization, Funding acquisition, Software, Supervision, Validation, Writing – review & editing. **Ming-Chih Lai:** Conceptualization, Formal analysis, Funding acquisition, Supervision, Validation, Writing – review & editing.

Declaration of competing interest

The authors declare that they have no known competing financial interests or personal relationships that could have appeared to influence the work reported in this paper.

Acknowledgement

The work of M.-C. Lai was supported in part by Ministry of Science and Technology of Taiwan under research grant MOST-110-2115-M-A49-011-MY3. The work of Y. Seol was supported by the basic science research program through the National Research Foundation of Korea (NRF) funded by the Korea government (NRF-2020R1A4A1018190).

Appendix A

In the immersed boundary framework, the rigid body surface is considered to be infinitesimally thin and treated as a singular force generator. To write the equations as a whole, the rigid body is filled with the internal fluid. The internal fluid effect has taken into account in Ω_s by considering the effective mass $M_e = (1 - \rho_f/\rho_s)M_s$ and effective moment of inertia tensor $\mathbf{I}_e = (1 - \rho_f/\rho_s)\mathbf{I}_s$ for the rigid body. As shown by [3], this internal fluid effect can be included in Equation (4) and Equation (5) as follows

$$\rho_s\,|\Omega_s|\,\frac{\mathrm{d}\mathbf{U}_c}{\mathrm{d}t} = -\int_{\partial\Omega_s} \mathbf{F}(\alpha,\beta,t)\mathrm{d}A + \rho_f \frac{\mathrm{d}}{\mathrm{d}t}\int_{\Omega_s} \mathbf{u}\mathrm{d}\mathbf{x} + \left(\rho_s - \rho_f\right)|\Omega_s|\,\mathbf{g}, \tag{22}$$

$$\mathbf{I}_s\frac{\mathrm{d}\boldsymbol{\omega}_c}{\mathrm{d}t} + \boldsymbol{\omega}_c \times \mathbf{I}_s\boldsymbol{\omega}_c = -Q^{\mathsf{T}}(t)\int_{\partial\Omega_s} (\mathbf{X}(\alpha,\beta,t) - \mathbf{X}_c) \times \mathbf{F}(\alpha,\beta,t)\mathrm{d}A + \rho_f\frac{\mathrm{d}}{\mathrm{d}t}Q^{\mathsf{T}}(t)\int_{\Omega_s} (\mathbf{X}(\alpha,\beta,t) - \mathbf{X}_c) \times \mathbf{u}\mathrm{d}\mathbf{x}. \tag{23}$$

Note that Equation (23) is the Euler rotation equation in a non-inertial frame in contrast to [3] which is expressed in an inertial frame. The Transport Theorem relates the time derivatives in an inertial frame to its time derivatives in a non-inertial frame. Following [3], we show the detail derivation of Equation (22) and Equation (23) to Equation (9) and (10), respectively, as follows. Here, the ρ_f and ρ_s have the same dimensionality. The rate-of-change term in Equation (22) holds for an incompressible fluid which satisfies a rigid-body motion in Ω_s as

$$\rho_f\frac{\mathrm{d}}{\mathrm{d}t}\int_{\Omega_s}\mathbf{u}\mathrm{d}\mathbf{x} = \rho_f\,|\Omega_s|\,\frac{\mathrm{d}\mathbf{U}_c}{\mathrm{d}t}. \tag{24}$$

Also, the internal fluid effect contributing to the Equation (23) is approximated by

$$\rho_f\frac{\mathrm{d}}{\mathrm{d}t}Q^{\mathsf{T}}(t)\int_{\Omega_s} (\mathbf{X}(\alpha,\beta,t) - \mathbf{X}_c) \times \mathbf{u}\mathrm{d}\mathbf{x} = \frac{\rho_f}{\rho_s}\left(\mathbf{I}_s\frac{\mathrm{d}\boldsymbol{\omega}_c}{\mathrm{d}t} + \boldsymbol{\omega}_c \times \mathbf{I}_s\boldsymbol{\omega}_c\right). \tag{25}$$

Substituting Equation (24) and Equation (25) into Equation (22) and Equation (23), respectively, yields

$$\left(1 - \frac{\rho_f}{\rho_s}\right)M_s\frac{\mathrm{d}\mathbf{U}_c}{\mathrm{d}t} = -\int_{\partial\Omega_s}\mathbf{F}(\alpha,\beta,t)\mathrm{d}A + \left(\rho_s - \rho_f\right)|\Omega_s|\,\mathbf{g}, \tag{26}$$

$$\left(1 - \frac{\rho_f}{\rho_s}\right)\left(\mathbf{I}_s\frac{\mathrm{d}\boldsymbol{\omega}_c}{\mathrm{d}t} + \boldsymbol{\omega}_c \times \mathbf{I}_s\boldsymbol{\omega}_c\right) = -Q^{\mathsf{T}}(t)\int_{\partial\Omega_s}(\mathbf{X}(\alpha,\beta,t) - \mathbf{X}_c) \times \mathbf{F}(\alpha,\beta,t)\mathrm{d}A. \tag{27}$$

Finally, discretizing Equation (26) and Equation (27) yields

$$M_e\frac{\mathbf{U}_c^{n+1} - \mathbf{U}_c^n}{\Delta t} = -\sum_{k=1}^{K}\mathbf{F}_k^{n+1}\Delta A(\mathbf{X}_k^n) + \left(\rho_s - \rho_f\right)|\Omega_s|\,\mathbf{g}, \tag{28}$$

$$\mathbf{I}_e\frac{\boldsymbol{\omega}_c^{n+1} - \boldsymbol{\omega}_c^n}{\Delta t} + \boldsymbol{\omega}_c^n \times \mathbf{I}_e\boldsymbol{\omega}_c^n = -\sum_{k=1}^{K}\boldsymbol{\Gamma}_k^0 \times Q^{\mathsf{T}}\mathbf{F}_k^{n+1}\Delta A(\mathbf{X}_k^n). \tag{29}$$

References

[1] C.S. Peskin, The immersed boundary method, Acta Numer. 11 (2002) 1–39.
[2] M.-C. Lai, C.S. Peskin, An immersed boundary method with formal second-order accuracy and reduced numerical viscosity, J. Comput. Phys. 160 (2000) 705–719.
[3] M. Uhlmann, An immersed boundary method with direct forcing for the simulation of particulate flows, J. Comput. Phys. 209 (2005) 448–476.
[4] N. Zhang, Z.C. Zheng, An improved direct-forcing immersed-boundary method for finite difference applications, J. Comput. Phys. 221 (2007) 250–268.
[5] M. Vanella, E. Balaras, A moving-least-squares reconstruction for embedded-boundary formulations, J. Comput. Phys. 228 (2009) 6617–6628.
[6] T. Kempe, J. Fröhlich, An improved immersed boundary method with direct forcing for the simulation of particle laden flows, J. Comput. Phys. 231 (2012) 3663–3684.

[7] S. Schwarz, T. Kempe, J. Fröhlich, A temporal discretization scheme to compute the motion of light particles in viscous flows by an immersed boundary method, J. Comput. Phys. 281 (2015) 591–613.
[8] S. Tschisgale, T. Kempe, J. Fröhlich, A non-iterative immersed boundary method for spherical particles of arbitrary density ratio, J. Comput. Phys. 339 (2017) 432–452.
[9] S. Tschisgale, T. Kempe, J. Fröhlich, A general implicit direct forcing immersed boundary method for rigid particles, Comput. Fluids 170 (2018) 285–298.
[10] Y. Kim, C.S. Peskin, A penalty immersed boundary method for a rigid body in fluid, Phys. Fluids 28 (2016) 033603.
[11] C. Wang, J.D. Eldredge, Strongly coupled dynamics of fluids and rigid-body systems with the immersed boundary projection method, J. Comput. Phys. 295 (2015) 87–113.
[12] U. Lācis, K. Taira, S. Bagheria, A stable fluid–structure-interaction solver for low-density rigid bodies using the immersed boundary projection method, J. Comput. Phys. 305 (2016) 300–318.
[13] A. Goza, T. Colonius, A strongly-coupled immersed-boundary formulation for thin elastic structures, J. Comput. Phys. 336 (2017) 401–411.
[14] L. Wang, C. Xie, W. Huang, A monolithic projection framework for constrained FSI problems with the immersed boundary method, Comput. Methods Appl. Mech. Eng. 371 (2020) 113332.
[15] T.-Y. Lin, H.-Y. Hsieh, H.-C. Tsai, A target-fixed immersed-boundary formulation for rigid bodies interacting with fluid flow, J. Comput. Phys. 429 (2021) 110003.
[16] K. Taira, T. Colonius, The immersed boundary method: a projection approach, J. Comput. Phys. 225 (2007) 2118–2137.
[17] T. Colonius, K. Taira, A fast immersed boundary method using a nullspace approach and multi-domain far-field boundary conditions, Comput. Methods Appl. Mech. Eng. 197 (2008) 2131–2146.
[18] J.S. Perot, An analysis of the fractional step method, J. Comput. Phys. 108 (1993) 51–58.
[19] R. Featherstone, Rigid Body Dynamics Algorithms, Springer US, 2008.
[20] J. Yang, F. Stern, A non-iterative direct forcing immersed boundary method for strongly-coupled fluid–solid interactions, J. Comput. Phys. 295 (2015) 779–804.
[21] F. Zhao, B.G.M. van Wachem, A novel quaternion integration approach for describing the behaviour of non-spherical particles, Acta Mech. 224 (2013) 3091–3109.
[22] P. Betsch, R. Siebert, Rigid body dynamics in terms of quaternions: Hamiltonian formulation and conserving numerical integration, Int. J. Numer. Methods Eng. 79 (2009) 444–473.
[23] A.J. Chorin, Numerical solution of the Navier-Stokes equations, Math. Comput. 22 (1968) 745–762.
[24] R. Temam, Sur l'approximation de la solution des équations de Navier-Stokes par la méthode des pas fractionnaires, Arch. Ration. Mech. Anal. 33 (1969) 377–385.
[25] Y. Saad, M.H. Schultz, GMRES: a generalized minimal residual algorithm for solving nonsymmetric linear systems, SIAM J. Sci. Stat. Comput. 7 (1986) 856–869.
[26] M.-C. Lai, W.-F. Hu, W.-W. Lin, A fractional step immersed boundary method for Stokes flow with an inextensible interface enclosing a solid particle, SIAM J. Sci. Comput. 34 (2012) B692–B710.
[27] M. Antuono, Tri-periodic fully three-dimensional analytic solutions for the Navier–Stokes equations, J. Fluid Mech. 890 (2019) A23.
[28] W.-P. Breugem, A second-order accurate immersed boundary method for fully resolved simulations of particle-laden flows, J. Comput. Phys. 231 (2012) 4469–4498.
[29] Z. Xia, K.W. Connington, S. Rapaka, P. Yue, J.J. Feng, S. Chen, Flow patterns in the sedimentatation of an elliptical particle, J. Fluid Mech. 625 (2009) 249–272.
[30] K. Suzuki, T. Inamuro, Effect of internal mass in the simulation of a moving body by the immersed boundary method, Comput. Fluids 49 (2011) 173–187.
[31] A. ten Cate, C.H. Nieuwstad, J.J. Derksen, H.E.A. Van den Akker, Particle imaging velocimetry experiments and lattice-Boltzmann simulations on a single sphere settling under gravity, Phys. Fluids 14 (2002) 4012–4025.
[32] G.B. Jeffrey, The motion of ellipsoidal particles immersed in a viscous fluid, Proc. R. Soc. Lond. 102 (1922) 161–179.